Constructing Diffeomorphic Representations of Non-Rigid Registrations of Medical Images

Carole Twining[1] and Stephen Marsland[1]

Imaging Science and Biomedical Engineering, University of Manchester
Manchester M13 9PT, U.K.

Abstract. The analysis of deformation fields, such as those generated by non-rigid registration algorithms, is central to the quantification of normal and abnormal variation of structures in the registered images. The correct choice of representation is an integral part of this analysis. This paper presents methods for constructing a general class of multi-dimensional diffeomorphic representations of deformations. We demonstrate that these representations are suitable for the description of deformations of medical images in 2 and 3 dimensions. Furthermore, we show that the non-Euclidean metric inherent in this representation is superior to the usual ad hoc Euclidean metrics in that it enables more accurate classification of legal and illegal variations.

1 Introduction

Non-rigid registration algorithms [4, 6, 12, 19] automatically generate dense (i.e., pixel-to-pixel or voxel-to-voxel) correspondences between pairs and sets of images with the aim of aligning analogous 'structures'. The deformation fields implicit in this correspondence contain information about the variability of structures across the set. In order to analyse quantitatively this variability, we need to be able to analyse the set of deformation fields. Such analysis must be based (either implicitly or explicitly) on a particular mathematical representation of the deformation field.

Previous work on the analysis of shape variability has used a range of representations; examples include polygonal [8] or spline [2] representations based on a small set of corresponding points (landmarks), Fourier representations [20] or spherical harmonics [3], medial based representations [17], or combinations of these [21]. The importance of the choice of representation has been demonstrated by the fact that explicitly optimizing the representation can lead to improved model performance [9]. Recent work on modelling dense 2D and 3D deformation fields has either used the densely-sampled deformation vectors directly (e.g., [13, 15]), or has employed a smooth, continuous representation of them (e.g., [18]). Neither of these methods guarantees that the deformation field is diffeomorphic (although B splines can be guaranteed diffeomorphic given certain non-trivial constraints on the control-point displacements [7]).

We contend that the appropriate representation should be continuous and diffeomorphic, as only a diffeomorphic representation allows an unambiguous one-to-one correspondence between all points in any pair of images. Where such

[1] Joint first authors. Email: {carole.twining,stephen.marsland}@man.ac.uk

a correspondence is not actually physically meaningful (e.g., in the case where additional structures such as tumours appear), this should be indicated by the warp parameters assuming atypical values. When we are considering the correspondence between discrete and bounded objects such as brains, it is also desirable that the warps themselves should be discrete and bounded. This leads us to suggest that a suitable representation is that of the group of continuous diffeomorphisms with some appropriate set of boundary conditions. Such a representation can be constructed using an approach based on Geodesic Interpolating Splines (GIS) [5]. In previous work [5, 16, 23] it has been shown that this approach also allows the construction of a metric on the diffeomorphism group.

In this paper, we demonstrate the construction of these diffeomorphic representations using a variety of spline bases. We show that these representations generate warps that are suitable for the task in hand, giving biologically 'plausible' warps in both two and three dimensions, whilst being of a relatively low dimensionality. We further study the significance of the metric (geodesic) distances between warps, and show that using it provides a measure of atypical variation that has greater discriminatory power than naïve measures based on the ad hoc use of a Euclidean metric on the space of warp parameters.

2 The Geodesic Interpolating Spline

2.1 Interpolating Splines

Consider a vector-valued spline function $\boldsymbol{f}(\boldsymbol{x})$, $\boldsymbol{x} \in \mathbb{R}^n$ that interpolates between data values at a set of knotpoints $\{\boldsymbol{x}_i : \ i = 1 \text{ to } N\}$, where $\boldsymbol{f}(\boldsymbol{x}_i) = \boldsymbol{f}_i$. We will restrict ourselves to the class of splines that can be expressed as the minimiser of a functional Lagrangian of the form:

$$E\left[\boldsymbol{f}\right] = \int_{\mathbb{R}^n} d\boldsymbol{x} \left\|L\boldsymbol{f}(\boldsymbol{x})\right\|^2 + \sum_{i=1}^{N} \lambda_i \left(\boldsymbol{f}(\boldsymbol{x}_i) - \boldsymbol{f}_i\right), \tag{1}$$

where L is some scalar differential operator. The first term in the Lagrangian is the smoothing term; the second term with the Lagrange multipliers $\{\lambda_i\}$ ensures that the spline fits the data at the knotpoints. The choice of operator L and boundary conditions defines a particular spline basis. The general solution can be written in the form:

$$\boldsymbol{f}(\boldsymbol{x}) = \boldsymbol{g}(\boldsymbol{x}) + \sum_{i=1}^{N} \boldsymbol{\alpha}_i G(\boldsymbol{x}, \boldsymbol{x}_i), \tag{2}$$

where:

$$\text{the affine function } g \text{ is a solution of: } L\boldsymbol{g}(\boldsymbol{x}) = 0, \tag{3}$$

$$\text{the Green's function } G \text{ is a solution of: } \left(L^\dagger L\right) G(\boldsymbol{x}, \boldsymbol{y}) \propto \delta(\boldsymbol{x} - \boldsymbol{y}), \tag{4}$$

and $L^\dagger$ is the Lagrange dual of L. In the table overleaf are a selection of commonly-used Green's functions. $\mathbb{D}^n$ is used to denote the unit ball in $\mathbb{R}^n$, and $\partial\mathbb{D}^n$ is its boundary.

The choice of Green's function depends on the boundary conditions and smoothness appropriate to the problem considered. For example, the CPS Green's function is useful for discrete objects such as brains, whereas an image of knee cartilage would require asymptotically linear boundary conditions.

Name	Dim	$L^\dagger L$	Boundary conditions on $f(\boldsymbol{x})$	$G(\boldsymbol{x},\boldsymbol{y})$
thin-plate [10] (TPS)	even	$(\nabla^2)^2$	asymptotically linear	$\|\boldsymbol{x}-\boldsymbol{y}\|^{4-n}\log\|\boldsymbol{x}-\boldsymbol{y}\|$
thin-plate [10] (TPS)	odd	$(\nabla^2)^2$	asymptotically linear	$\|\boldsymbol{x}-\boldsymbol{y}\|^{4-n}$
biharmonic clamped plate [1, 23] (CPS)	2	$(\nabla^2)^2$	$f=f'=0$ on and outside $\partial\mathbb{D}^2$	$\|\boldsymbol{x}-\boldsymbol{y}\|^2\left(A^2-1-\log A^2\right)$, $A(\boldsymbol{x},\boldsymbol{y})=\frac{\sqrt{\boldsymbol{x}^2\boldsymbol{y}^2-2\boldsymbol{x}\cdot\boldsymbol{y}+1}}{\|\boldsymbol{x}-\boldsymbol{y}\|}$
triharmonic clamped plate [1] (CPS)	3	$(\nabla^2)^3$	$f=f'=0$ on and outside $\partial\mathbb{D}^3$	$\|\boldsymbol{x}-\boldsymbol{y}\|\left(A+\frac{1}{A}-2\right)$, $A(\boldsymbol{x},\boldsymbol{y})=\frac{\sqrt{\boldsymbol{x}^2\boldsymbol{y}^2-2\boldsymbol{x}\cdot\boldsymbol{y}+1}}{\|\boldsymbol{x}-\boldsymbol{y}\|}$
Gaussian	n	$\exp\left(-\frac{\nabla^2}{4\beta}\right)$	asymptotically linear	$\exp\left(-\beta\|\boldsymbol{x}-\boldsymbol{y}\|^2\right)$

2.2 The Affine Function

Taking the general form of $\boldsymbol{f}(\boldsymbol{x})$ given above, and substituting into equation (1), we obtain:

$$E\left[\{\boldsymbol{\alpha}_k\}\right]=\sum_{i,j}G(\boldsymbol{x}_i,\boldsymbol{x}_j)\boldsymbol{\alpha}_i\cdot\boldsymbol{\alpha}_j=G_{ij}\boldsymbol{\alpha}_i\cdot\boldsymbol{\alpha}_j.^{1} \tag{5}$$

The spline coefficients $\{\boldsymbol{\alpha}_i\}$ and the affine function (see equation (3)) are then obtained by optimising this form of the energy function with the set of constraints $\boldsymbol{g}(\boldsymbol{x}_i)=G_{ij}\boldsymbol{\alpha}_j-\boldsymbol{f}_i$.

For operators where the boundary conditions are that the deformation is asymptotically linear, the affine function is the general linear function; using the notation of Camion and Younes [5], this can be written (in n dimensions) in the form:

$$Q=\begin{pmatrix}x_1^1 & x_1^2 & \dots & x_1^n & 1\\ & & \vdots & & \\ x_N^1 & x_N^2 & \dots & x_N^n & 1\end{pmatrix},\ g^\mu(\boldsymbol{x}_i)=Q_{ia}\gamma_a^\mu,\ \mu=1,\dots,n;\ a=1,\dots,n+1, \tag{6}$$

where $\{x_i^\mu\}$ are the coordinates of the ith knotpoint, and the affine parameters $\{\gamma_a^\mu\}$ are combinations of the scaling parameter, the rotation angle(s), and the coordinate translations. Solving for $\{\boldsymbol{\alpha}_i\}$ and $\{\gamma_a^\mu\}$, we then obtain:

$$\gamma_a^\mu=\left(Q^TG^{-1}Q\right)^{-1}_{ab}Q^T_{bi}G^{-1}_{ij}f_j^\mu,\ \ \alpha_i^\mu=G^{-1}_{ij}\left(f_j^\mu-Q_{ja}\gamma_a^\mu\right).^{2} \tag{7}$$

For the case of the clamped-plate spline, we will take the affine function to be that defined in equation (3), with the boundary conditions being imposed *after* the affine alignment.

Let us now consider using the splines defined above to represent the densely-sampled deformation field of an image, where a point at original position $\boldsymbol{x}$ is

[1] We adopt the summation convention that we sum over repeated indices.

[2] Note that the expression for γ_a^μ differs from [5], where there is a typographical error and the second factor of G^{-1} has been omitted.

warped to a position $\boldsymbol{x} + \boldsymbol{f}(\boldsymbol{x})$. There will be some set of knotpoints (with associated initial and final positions) and knotpoint displacements for which the interpolated displacement field exactly matches our given displacement field at all sample points. We will call such a set of knotpoints and knotpoint displacements a representation of the deformation field $\boldsymbol{f}(\boldsymbol{x})$. However, such an interpolated deformation field is only guaranteed to be diffeomorphic in the limit of sufficiently small displacements (see Fig. 1, plots (iii) and (vi) for examples).

2.3 Geodesic Interpolating Splines

The usual approach to constructing a large-deformation diffeomorphism is to consider such a deformation as an infinite sequence of infinitesimal deformations [5, 11, 14, 22]; that is, we have an infinite sequence of the spline-part generated by the Green's function G, and an infinite sequence of infinitesimal affine transformations. We have a flow-time t, where our knotpoints now follow paths $\{\boldsymbol{x}_i(t); t \in [0; 1]\}$, with an associated energy (the generalisation of equation (5)):

$$E\left[\boldsymbol{\alpha}_k(t)\right] = \int_0^1 dt\, G\left(\boldsymbol{x}_i(t), \boldsymbol{x}_j(t)\right)\left(\boldsymbol{\alpha}_i(t) \cdot \boldsymbol{\alpha}_j(t)\right). \tag{8}$$

The spline parameters $\{\boldsymbol{\alpha}_i(t)\}$ and the affine parameters $\{\gamma_i^\mu(t)\}$ are now related by the obvious generalisation of equation (7), where the displacements $\{f_i^\mu\}$ are replaced by the velocities of the knotpoints $\left\{v_i^\mu(t) = \frac{dx_i^\mu(t)}{dt}\right\}$. Note that we no longer have an exact solution, since the knotpoint paths are only constrained at their end-points. We therefore have to numerically optimise the expression for the energy in equation (8), where the free variables are the knotpoint paths between their fixed end points. We use the optimisation scheme previously described in [23]. For an example of the *curved* optimised paths, see Fig. 1.

As in section 2.2, we take the initial and final knotpoint positions to be a representation of the diffeomorphism generated by the interpolation. We denote such a geodesic interpolating spline (GIS) diffeomorphism by $\omega(\{\boldsymbol{x}_i(0)\}, \{\boldsymbol{x}_i(1)\})$. As was shown by Camion and Younes [5], who considered using the GIS for inexact landmark matching, the optimised value for the energy has the important property that it can be considered as the square of a geodesic distance function d on the group of diffeomorphisms. That is, $E_{opt}(\omega) = d^2(e, \omega)$, where e is the identity element of the group. This distance function has the important property that it is invariant under (left-) multiplication by an arbitrary group element [5]. This means that, if we are considering the pairwise geodesic distances between a set of warps generated by non-rigid registration of a set of images, then the calculated distances are independent of the choice of reference image. We also note that this metric provides us with a principled way of defining warps that interpolate between any two given warps [23]; the flow in the space of diffeomorphisms gives a geodesic on the space of warps, and the geodesic distance allows us to calculate a warp on this geodesic halfway between the two initial warps.

As an example, we consider the diffeomorphisms generated by the motion of a small set of knotpoints with random displacements. We use the Gaussian Green's function with a fixed value of the parameter β. The initial knotpoint positions are shown in plot (i) of Fig. 1. For each random set of knotpoint displacements, we

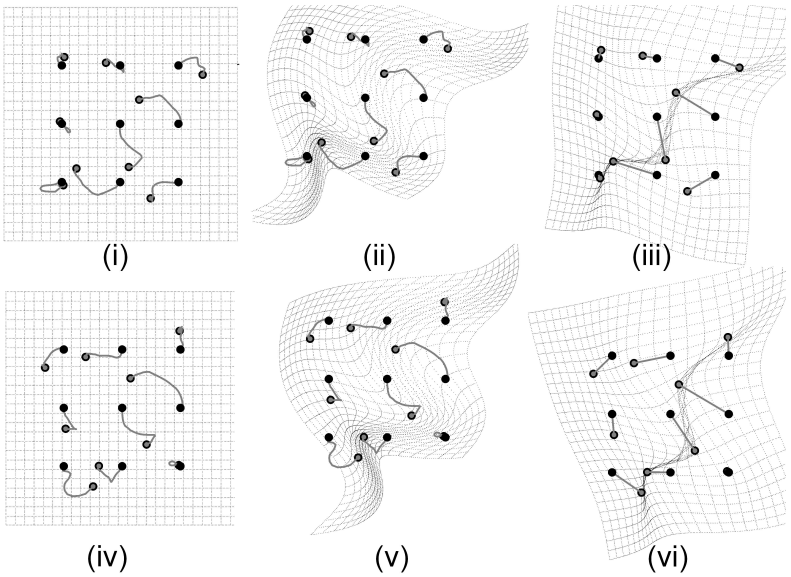

Fig. 1. Example random displacements with geodesic and non-geodesic spline interpolants. (i) Initial knotpoints positions (black circles), final positions (grey circles) and the knotpoint paths (grey lines). (ii) The GIS Gaussian warped image and knotpoints. (iii) The non-geodesic thin-plate spline warp. (iv) The rotated displacements. (v) The GIS Gaussian warp. (vi) The non-geodesic thin-plate spline warp.

also consider the same displacements, but with an added affine transformation of a rotation of $\frac{\pi}{8}$ about the central point (shown in plot (iv) in the figure). This additional part of the transformation should not affect the computed geodesic distance of this warp from the identity as it is purely affine, and the additional affine part of the transformation should appear in the flow in the space of affine functions. The GIS warped versions of the grids are shown in plots (ii) and (v). For comparison, we also give the thin-plate spline interpolant (plots (iii) and (vi)) of the same deformation fields (i.e., NOT the geodesic interpolating spline). It can be seen clearly that both these non-geodesic warps fold and are therefore not diffeomorphic, in contrast to both of the GIS warps (plots (ii) and (v)), which do not fold, despite the large knotpoint displacements.

We compared the computed geodesic distances for a set of 98 random displacements with and without a rotation. The computed geodesic distances ranged from 0.05 to 0.9 across the set of examples. It was found that the geodesic distances with and without rotation were almost identical for all 98 examples, with a mean fractional difference between the values of less than 2%, and a correlation coefficient between the values of 0.9982; we would not have expected the values to be absolutely identical, given the numerical errors inherent in the finite-dimensional representation of the knotpoint paths.

3 Representing Diffeomorphisms

3.1 Representing 2D Diffeomorphisms

When considering warps of 2D biological images, it is obviously important that the generated warps are not only diffeomorphic, but also biologically plausible. To investigate this, we considered a set of 2D T1-weighted MR axial slices of

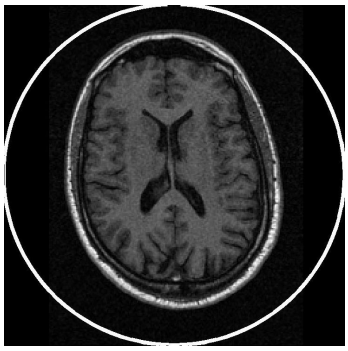

Fig. 2. An example 2-D brain slice with the bounding circle.

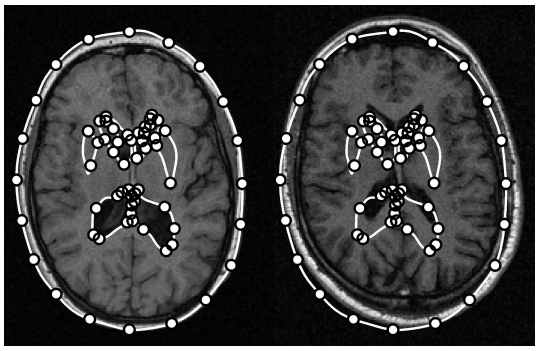

Fig. 3. *Left:* Annotation (white line) and knotpoints (white circles) on the original brain slice. *Right:* The same knots positioned on another brain slice.

brains, where the slices chosen show the lateral ventricles. For each image, the positions of the lateral ventricles and the skull were annotated by a radiologist using a set of 163 points. We took a subset of 66 of these points to be the positions of our knots (see Fig. 3). Given a pair of images, the knotpoint positions on the images give us the initial and final positions of our knotpoint paths. We then calculated the geodesic interpolating spline warp corresponding to these positions using the 2D clamped-plate spline as Green's function. The bounding circle for the spline is as shown in Fig. 2.

Note that we did not affinely align the knots before calculating the warp; hence the algorithm has to deal with a non-trivial pseudo-affine part. Including the affine part would have made the task easier. Example results are shown in Fig. 4. It can be seen that the warps are indeed diffeomorphic, and appear to be very smooth – each of the brain slices still looks biologically plausible, which would not be true had a simpler scheme been used. The warped images are not resampled – the images are instead plotted as coloured surfaces, so that the size and position of each warped pixel is retained. The pairs of images were chosen to illustrate cases where the required deformation was considerable, both in terms of the change in shape of the ventricles and skull, and in terms of the difference in scale and orientation of the slice as a whole. The resultant warped images do indeed appear to be biologically plausible, despite the relatively low dimensionality of the representation used – structures other than the labelled ones have been brought into approximate alignment. This suggests that a dense correspondence (for instance, one given by a non-rigid registration using maximisation of mutual information) could also be represented by these warps without an inordinate increase in the dimensionality of the representation.

3.2 Representing 3D Diffeomorphisms

We have shown that this geodesic interpolating spline basis can generate biologically plausible warps in 2D; we now proceed to show that we can also do the same in 3D. Furthermore, we need to show that given a warp, we can choose the knotpoints appropriately. To do this, we consider a set of segmented hippocampi. Each example consists of a triangulated surface with 268 vertices, where the

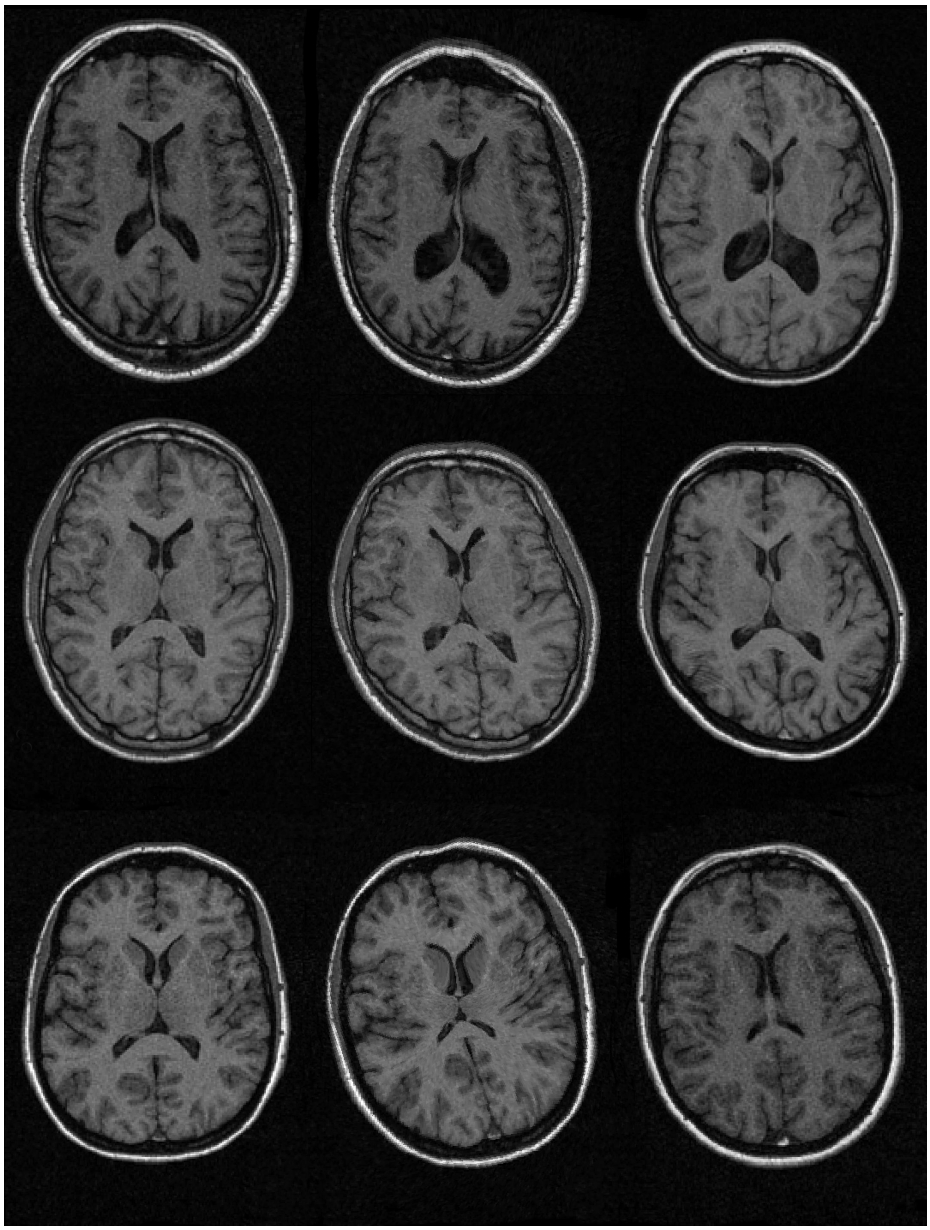

Fig. 4. Three examples of warp interpolation using the clamped-plate spline. Pixel intensity is unchanged, but note that the image structures are approximately aligned. *Left:* Source image, *Centre:* Warped image, *Right:* Target image.

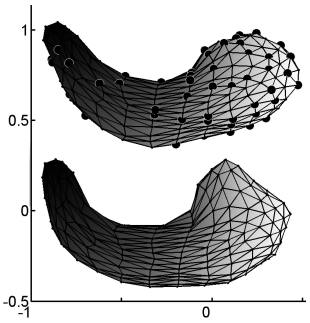

Fig. 5. Target (bottom) and source (top) hippocampi with knotpoints (black circles). The correspondence between the shapes is indicated by the shading.

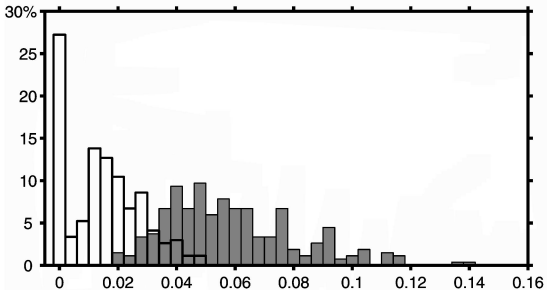

Fig. 6. Distribution of point discrepancy between source and target (grey bars), and warped source and target (white bars). Units as in Fig. 5.

vertices for each example have been manipulated to give the optimised correspondence [9]. Examples are shown in Fig. 5. Pairs of hippocampi were chosen at random, and the 2 shapes aligned using generalised Procrustes analysis. We used the triharmonic clamped-plate spline (see section 2.1) as our GIS basis, each hippocampus being scaled to fit within the unit sphere. The required warp between source and target was calculated iteratively – the warp was optimised for a given set of knotpoints, then new knotpoints added and the warp recalculated. New knotpoints are selected from the vertices using a greedy algorithm: the discrepancy between the vertices of the warped source and the target are calculated, and new knotpoints are then selected from those vertices that have the largest discrepancies.

Fig. 6 shows the distribution of the discrepancies between the aligned source and target, and the final warped source and target, for a set of 70 knotpoints. It can be seen that the distribution of discrepancies as a whole has been shifted towards smaller values. In Fig. 7, we show the maximum, median and mean-square discrepancies for non-knot points only as a function of the number of knotpoints for 4 random pairs of hippocampi. Note that the nature of our greedy algorithm for selecting knotpoints means that the maximum discrepancy is not

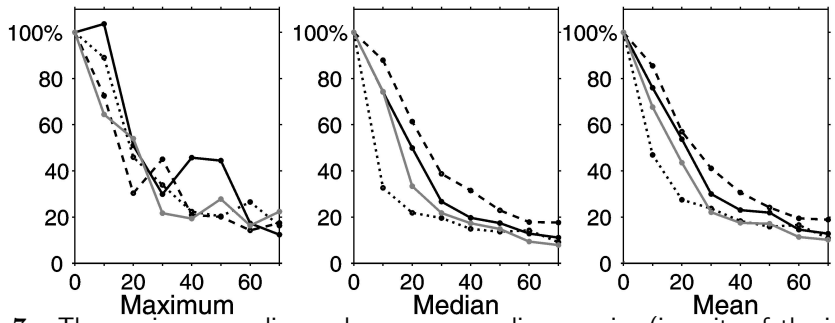

Fig. 7. The maximum, median and mean square discrepancies (in units of the initial discrepancy), for non-knot points only, as a function of the number of knots. Data is shown from 4 randomly selected pairs of hippocampi.

guaranteed to decrease monotonically. However, all three graphs show that the algorithm quickly reaches a reasonable representation of the required warp, for a number of knotpoints that is approximately 25% of the number of vertices.

4 Modelling Discrete Structures

4.1 A Simple Example

There are numerous examples in biological and medical images of cases where a pair of structures remain discrete, although the spacing between them varies considerably across a population, for example, the lateral ventricles in the brain. We constructed a simple dataset to investigate the problems associated with modelling such a variation, the basic idea of which is shown in Fig. 8. Elements of the dataset comprise 6 points defining two triangles, with the separation s between the two triangles constrained to remain positive. A training set of 100 examples was generated, with the separation s being chosen at random. A standard method for analysing such a dataset is to build a statistical shape model (SSM) [8]; the training set was Procrustes aligned, and a linear SSM constructed.

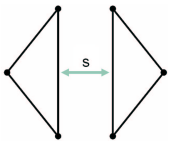

Fig. 8. The distance s between the discrete structures varies.

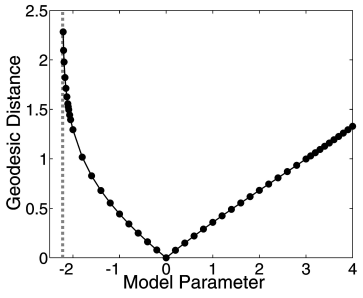

Fig. 9. Geodesic distance versus model parameter for the discrete structure dataset.

The model correctly displayed only one mode of variation; example shapes generated by the model are shown in Fig. 10. As was expected, this simple linear model can generate illegal shapes – when the model parameter went below a threshold of approximately -2.22 standard deviations, the triangles intersected, so that the structures were no longer discrete. This was not seen in the training set and therefore should not be allowed. We then calculated the CPS geodesic warps generated by taking the 6 points that define each pair of triangles as knotpoints and warping between examples generated by the model for varying model parameter and the model mean shape. The CPS was a suitable choice of Green's function because the triangles are discrete objects. The variation of the geodesic distance from the mean shape, plotted against the model parameter (which is equivalent to the Mahalanobis distance, a distance defined by imposing a Euclidean metric on the space of point positions) is shown in Fig. 9. Positive values of the model parameter, which correspond to increasing separation of the triangles, show a relationship between model parameter and geodesic distance that is very close to linear, but for negative values of the parameter (decreasing separation), the geodesic distance diverges at the precise value of the parameter that corresponds to zero separation. The geodesic distance therefore allows us to differentiate between physical and non-physical variations in a way that naïve linear models cannot.

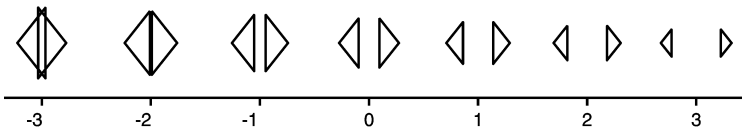

Fig. 10. Example shapes generated from the SSM model of the discrete structures dataset for varying model parameter (Mahalanobis distance). The change in scale as the model parameter varies is caused by the fact that the points have been Procrustes aligned.

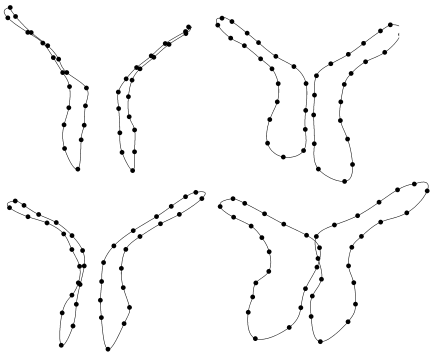

Fig. 11. *Top:* Examples from the training set. *Bottom:* Legal (left) and illegal (right) examples generated by the SSM. Knotpoints are indicated by black circles; lines are for the purposes of illustration.

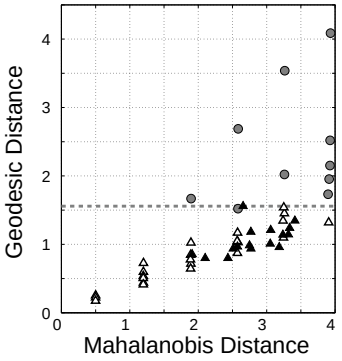

Fig. 12. Mahalanobis vs. geodesic distances from the mean shape for *grey circles:* illegal shapes generated by the SSM, *white triangles:* legal shapes generated by the SSM, *black triangles:* the training set.

4.2 Using the Geodesic Distance to Classify Variations

We now consider the role of the geodesic distance in classifying legal and illegal variations in real biological data. We take as our dataset the annotated outlines of the anterior lateral ventricles as used in section 3.1 in the axial brain slices. Each example consists of 40 knotpoints (see Fig. 11). The set of training examples was Procrustes aligned and then scaled to fit inside the unit circle. A linear SSM was built from this training set in the usual way. We then used this SSM to generate random example shapes. These examples were classified as legal if the outlines of both ventricles did not intersect either themselves or each other, and illegal otherwise. The training set of shapes are, by definition, legal.

We then calculated the GIS warps, using the biharmonic CPS basis, between the classified set of shapes and the mean shape from the model. The geodesic distance from the mean is compared with the Mahalanobis distance from the mean in Fig. 12. It is immediately obvious that we cannot separate the legal and illegal shapes by using the Mahalanobis distance from the mean. However, using the geodesic distance, it is possible to construct a simple classifier (shown by the dotted grey line) that separates the two groups, with only one example shape being misclassified (the grey circle just below the line). Given that the Mahalanobis distance for the SSM is equivalent to a Euclidean metric on the space of point deformations, this again demonstrates the superiority of the GIS metric over an ad hoc metric.

The correspondences that we have used in this example are a subset of the correspondences that we would expect to be generated by a successful non-rigid registration of the images. Increasing the density of points on the training shapes would have left the result for the Mahalanobis distance essentially unchanged. However, the result for the GIS warp would have improved, giving a greater separation between the two sets of shapes. This is because, in the limit where the lines become infinitely densely sampled, it is actually impossible to construct a diffeomorphism for which the lines cross, which would mean that the geodesic distance for the illegal shapes would approach infinity as the sampling density increased. We can now extend this result to the case of modelling the deformation fields for the non-rigid registration; a linear model of such deformation fields would suffer the same problem as the linear SSM, where now the overlapping structures would correspond to a folding of the warp. The GIS cannot, by definition, generate such a folding since it is guaranteed to be diffeomorphic.

5 Conclusions

This paper has introduced a principled diffeomorphic representation of deformation fields with an inherent non-Euclidean metric. The spline basis of this representation is defined by the choice of Green's function and boundary conditions, which can be altered to suit the particular task in hand. We have demonstrated that this representation method can accurately represent real biological variations in both two and three dimensions.

Conventional linear modelling strategies impose a Euclidean metric on the space of parameters (in our case, the knotpoint positions). The Mahalanobis distance that we have used for comparisons in this paper is derived from such a metric. The example in section 4.2 clearly shows the superiority of the non-Euclidean metric in quantifying variation.

Acknowledgements

Our thanks to G. Gerig and M. Steiner for the hippocampus dataset, and to Rh. Davies for providing us with his optimised correspondences for this dataset. This research was supported by the MIAS IRC project, EPSRC grant number GR/N14248/01.

References

1. T. Boggio. Sulle funzioni di green d'ordine m. *Rendiconti - Circolo Matematico di Palermo*, 20:97–135, 1905.
2. F. L. Bookstein. Principal Warps: Thin-Plate Splines and the Decomposition of Deformations. *IEEE Transactions on Pattern Analysis and Machine Intelligence*, 11(6):567–585, 1989.
3. Ch. Brechbuehler, G. Gerig, and O. Kuebler. Parametrization of closed surfaces for 3D shape description. *Computer Vision and Image Understanding*, 61(2):154–170, 1995.
4. M. Bro-Nielsen and C. Gramkow. Fast fluid registration of medical images. In *Proceedings of Visualization in Biomedical Computing (VBC)*, pages 267–276, 1996.
5. V. Camion and L. Younes. Geodesic interpolating splines. In M. Figueiredo, J. Zerubia, and A. K. Jain, editors, *Proceedings of EMMCVPR'01*, volume 2134 of *Lecture Notes in Computer Science*, pages 513–527. Springer, 2001.

6. C. Chefd'Hotel, G. Hermosillo, and O. Faugeras. A variational approach to multi-modal image matching. In *Proceedings of IEEE Workshop on Variational and Level Set Methods (VLSM'01)*, pages 21 – 28, 2001.
7. Y. Choi and S. Lee. Injectivity conditions of 2D and 3D uniform cubic B spline functions. *Graphical Models*, 62(6):411–427, 2000.
8. T. F. Cootes, C. J. Taylor, D. H. Cooper, and J. Graham. Active shape models – their training and application. *Computer Vision and Image Understanding*, 61(1):38–59, 1995.
9. Rh. Davies, C. J. Twining, T. F. Cootes, J. C. Waterton, and C. J. Taylor. 3D statistical shape models using direct optimisation of description length. In *Proceedings of the 7th European Conference on Computer Vision (ECCV)*, volume 2352 of *Lecture Notes in Computer Science*, pages 3–20. Springer, 2002.
10. J. Duchon. Interpolation des fonctions de deux variables suivant le principe de la flexion des plaques minces. *Revue Française d'Automatique, Informatique, Recherche Opérationelle (RAIRO) Analyse Numerique*, 10:5–12, 1976.
11. P. Dupuis, U. Grenander, and M. I. Miller. Variational problems on flows of diffeomorphisms for image matching. *Quarterly of Applied Mathematics*, 56(3):587–600, 1998.
12. J. Gee, M. Reivich, and R. Bajcsy. Elastically deforming 3D atlas to match anatomical brain images. *Journal of Computer Assisted Tomography*, 17(2):225–236, 1993.
13. A. Guimond, J. Meunier, and J.-P. Thirion. Average brain models: A convergence study. Technical Report RR-3731, INRIA, Sophia Antipolis, 1999.
14. S. C. Joshi and M. M. Miller. Landmark matching via large deformation diffeomorphisms. *IEEE Transactions on Image Processing*, 9(8):1357–1370, 2000.
15. L. LeBriquer and J. Gee. Design of a statistical model of brain shape. In *Proceedings of IPMI'97*, volume 1230 of *Lecture Notes in Computer Science*, pages 477–482. Springer, 1997.
16. S. Marsland and C. J. Twining. Clamped-plate splines and the optimal flow of bounded diffeomorphisms. In *Statistics of Large Datasets, Proceedings of Leeds Annual Statistical Research Workshop*, pages 91–95, 2002.
17. S. M. Pizer, D. S. Fritsch, P. Yushkevich, V. Johnson, and E. Chaney. Segmentation, registration, and measurement of shape variation via image object shape. *IEEE Transactions on Medical Imaging*, 18(10):851–865, 1999.
18. D. Rueckert, A. F. Frangi, and J. A. Schnabel. Automatic construction of 3D statistical deformation models using non-rigid registration. In *Proceedings of MICCAI'01*, volume 2208 of *Lecture notes in Computer Science*, pages 77–84, 2001.
19. D. Rueckert, L. I. Sonoda, C. Hayes, D. L. G. Hill, M. O. Leach, and D. J. Hawkes. Non-rigid registration using free-form deformations: Application to breast MR images. *IEEE Transactions on Medical Imaging*, 18(8):712–721, 1999.
20. L. H. Staib and J. S. Duncan. Boundary finding with parametrically deformable models. *IEEE Transactions on Pattern Analysis and Machine Intelligence*, 14(11):1061–1075, 1992.
21. M. Styner and G. Gerig. Hybrid boundary-medial shape description for biologically variable shapes. In *Proceedings of IEEE Workshop on Mathematical Methods in Biomedical Image Analysis (MMBIA) 2000*, pages 235–242, June 2000.
22. A. Trouvé. Diffeomorphisms groups and pattern matching in image analysis. *International Journal of Computer Vision*, 28(3):213–221, 1998.
23. C. J. Twining, S. Marsland, and C. J. Taylor. Measuring geodesic distances on the space of bounded diffeomorphims. In *Proceedings of BMVC'02*, volume 2, pages 847–856. BMVA Press, 2002.